Numerical Investigation of Laser Absorption by Metal Powder Bed in Selective Laser Sintering Processes

Xuxiao Li and Wenda Tan

Department of Mechanical Engineering, University of Utah, Salt Lake City, UT 84112
Corresponding Author Email: wenda.tan@mech.utah.edu

ABSTRACT

Laser absorption by powder bed in selective laser sintering (SLS) processes remains a critical issue to be fully understood. This issue is important for the appropriate selection of processing parameters in practices as well as an accurate definition of the thermal input in numerical modeling. In this work, a ray tracing model is used to study this issue. In parametric studies, the effects of laser parameters and powder bed structures on the laser absorption are investigated. It is found that a top-hat laser produces a more uniform laser absorption within laser heated spots than a Gaussian laser. The absorption distribution generally does not follow an exponential decay; instead, it gradually increases to a "peak" and then decreases along the laser shooting direction. The absorption near the substrate can be enhanced when the powder bed thickness is reduced, which helps to bind the newly deposited layer with its substrate in SLS processes. Finally, using bimodal powder beds can reduce laser penetration and produce more uniform laser absorption in laser heated spots.

Keywords: selective laser sintering, laser absorption, powder bed, ray tracing method.

1 INTRODUCTION

Selective laser sintering (SLS) is a promising manufacturing process that is capable of manufacturing parts with complex geometry for a wide range of materials. In SLS, a laser beam scans across a pre-deposited powder bed (PB) and builds parts by selectively fusing powder in a layer-by-layer fashion [1]. As a laser illuminates the PB, it transfers energy to the powders through multiple-reflections, producing a three-dimensional absorption inside the PB. An understanding of the absorption distribution is important for optimizing process parameters to achieve a more efficient and uniform laser absorption. It is also important for the modeling of SLS processes, because the absorption acts as a heat source for the ensuing heat conduction in the PB. In many of the existing simulations [2-4], the absorption distributions are described by $q(x,y,z)$, which is a function of position and in the unit of W/m^3. It takes the general form of Eqn. 1,

$$q(x,y,z) = f(x,z)g(y) \quad (1)$$

, where the x-z plane is the horizontal plane and the y axis is perpendicular to the x-z plane; $f(x,z)$ is a function representing the laser power profile, usually of a bell-like shape for Gaussian lasers; $g(y)$ is a function describing the laser penetration into the PB which decays in an exponential fashion. A detailed derivation of $g(y)$ using the radiative transfer equation and the two-flux model is given in [3].

The above model (Eqn. 1) for laser absorption assumes that the PB, in an average manner, is a homogeneous material such that the energy transfer can be described by differential equations that lead to a continuous absorption distribution in the PB. However, the PB by nature is "discrete": laser can be directly transmitted through the gaps between powder particles; the absorbed power tends to concentrate at powder surfaces, instead of continuously distributing within the powders. These discrete effects become more salient when the laser spot is comparable to powder particles in size and therefore defy the "continuous" model. It has been demonstrated in [5] that the attendant physics phenomena simulated by different laser absorption models can be very different.

The ray tracing method has been adopted to calculate the energy transfer between the laser and the material in laser keyhole welding [6-9], laser cladding [10], and SLS [11-14]. In [11-14], a PB consisting of opaque spherical particles is first generated; then the laser beam is divided into many "rays", each having a certain size, direction, and amount of power. Upon an incidence of a ray on a particle's surface, a portion of its power is absorbed and the ray is reflected, governed by the laws of geometric optics. By tracking each ray's multiple reflections through the PB in this fashion, the absorption distribution can be calculated. It is worth mentioning that the geometric optics is only valid when Eqn. 2 is satisfied [15].

$$2\pi a \gg \lambda \tag{2}$$

Here a is the particle size parameter and λ is the wavelength of the laser. When the wavelength and particle size are of the same magnitude, laser scattering and diffraction become significant, leading to the failure of geometric optics.

Compared with the continuous model, the ray tracing model more accurately describes the laser absorption by accounting for the discrete particle geometry of the PB. However, in the existing literature, there is a lack of the discussion about more realistic scenarios as those encountered in SLS. Studies in [12-14] have focused on the absorption of very thick PB such that the absorption diminishes near the bottom of the PB, while in SLS the PB should be relatively thin so that the bottom of the PB and the substrate underneath can both absorb adequate energy to be bound. There is also a lack of details about the absorption distribution in the PB. In [11] the absorptivity of the PB is studied, but the distribution of absorption within the PB is not discussed. In [12-14] the absorption distribution along the laser shooting direction is studied, but no quantitative results are given about the distribution in the dimensions transverse to the laser shooting direction. In this paper, a random pack algorithm generates the PB, and a ray tracing model is applied to calculate the laser absorptions by the PB in SLS processes. More details of the absorption distribution in the PB are provided, and the effects of laser parameters and PB structures on the laser absorption are examined.

2 MODEL DESCRIPTION

2.1 Powder Bed Generation

The Probabilistic-Analytic Consecutive Kinetic Simulation (PACKS) [16] is used to generate randomly packed PB. In the PACKS, the powder particles are considered as spheres of different sizes and they are sequentially dropped into a cuboid container from a random initial position high above the container. Once a particle is dropped, it rolls down the existing particles

until it reaches a stable position where a particle either touches the floor or it is supported by three existing particles. Once a particle reaches a stable position, this particle stays at that position, not affected by the particles dropped later. To control the thickness of powder bed, when a particle reaches a stable position higher than the defined powder bed thickness, this particle is eliminated and another different particle is dropped. The dropping process stops when the number of the eliminated particles is three times that of the existing particles in the PB. An example of the PB generated by the PACKS is shown in Fig. 1.

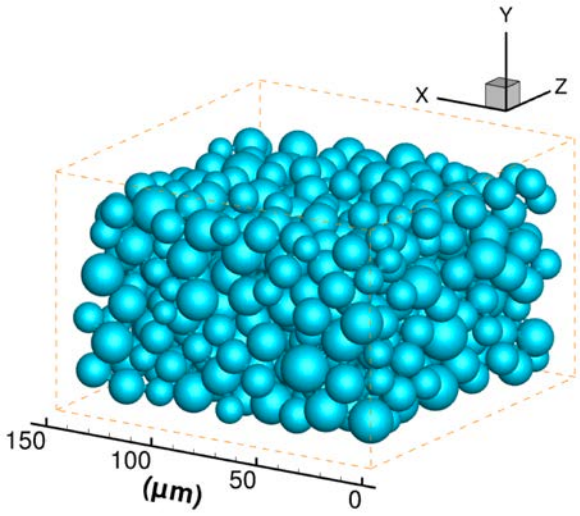

Fig. 1. Example of powder bed generated by PACKS.

2.2 Ray Tracing Model

In the ray tracing model, the laser is divided into rays and shot vertically towards the PB (along the y direction defined in Fig. 1). Each ray is assigned with a certain size, a direction, and amount of power. Upon the incidence of a ray on the surface of a particle, a portion of its power is absorbed by the particle surface and the remainder power goes to the reflected ray. The law of reflection determines the direction of the reflected ray, and the absorptivity is calculated by Eqn. 3) [17],

$$A(\gamma) = 1 - \frac{1}{2}\left[\frac{(n\cos\gamma - 1)^2 + k^2\cos^2\gamma}{(n\cos\gamma + 1)^2 + k^2\cos^2\gamma} + \frac{(n - \cos\gamma)^2 + k^2}{(n + \cos\gamma)^2 + k^2}\right] \quad (3)$$

, where γ is the incident angle; n and k are the optical constants of the material as summarized in Table 1. Fig. 2 shows the absorptivity as a function of incident angle for stainless steel (SS) and copper (Cu) at a laser wavelength of 1000nm. It is observed that the absorptivity slightly increases with the incident angle until it reaches the maximum, and then the absorptivity dramatically decreases to zero as the incident angle approaches 90 degrees. When a ray hits the bottom of the PB, where a substrate surface resides, it is reflected in a random direction to simulate the reflection on an uneven substrate surface. For each case to be studied, 30 simulations will be run on different PBs randomly generated with the same particle size distribution to account for the inherent randomness of the PB structure.

Table 1. Optical constants used in current simulations

Material	Laser wavelength (nm)	n	k
Stainless steel [11]	1000	3.24	4.28
Copper [18]	1000	0.54	6.53
	790	0.44	4.90
	633	0.58	3.65
Iron [18]	790	2.99	3.61
	633	2.87	3.36

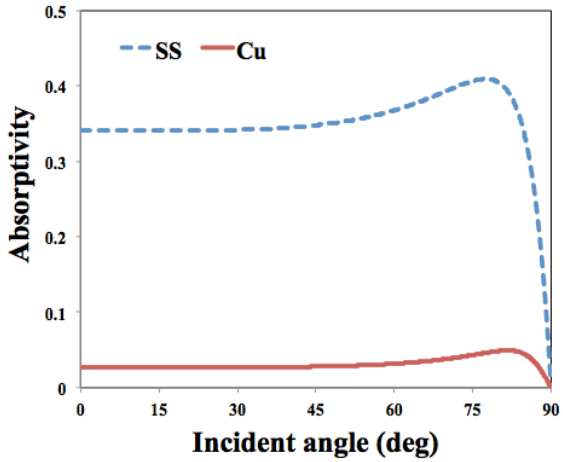

Fig. 2. Absorptivity dependency on incident angle.

3 MODEL EXAMINATION

3.1 Sensitivity Analysis

To study the effect of ray size on the accuracy of the ray tracing simulation results, the laser absorption of a single powder particle is simulated. A stainless steel particle of radius 30 μm is positioned at the center of a 100×100×100 μm^3 cube calculation domain (CD). As shown in Fig. 3a, a fiber laser is shot from the top of the CD towards the particle (along y direction) with a uniform power density distribution (i.e. top-hat distribution), and will pass through the bottom of CD without being reflected. The upper half of the particle surface is exposed to the laser illumination and absorbs laser power. To study the absorption distribution in more details, the particle surface is divided into segments called "zones" (Fig. 3b). The absorbed power density in a zone, $I_{abs,z}$, is calculated as the total power absorption in this zone divided by the zone area, S_z. The distribution of ratio I_{abs}/I_0 is shown in Fig. 3a, with I_0 being the power density of the incident laser. The top portion of the particle receives higher power density than the surrounding portion. This is because the absorbed power density of each zone can be calculated theoretically by Eqn. 4.

$$\bar{I}_{abs,\,z} = \frac{1}{S_z} \iint_{\text{zone}} I_0 A(\gamma) \cos\gamma \, dS \tag{4}$$

The zones in the top portion of the particle usually have smaller incident angles than the zones in the surroundings, which generally gives larger values for the multiplication of $A(\gamma)\cos\gamma$ in Eqn. 4, and hence a higher power density.

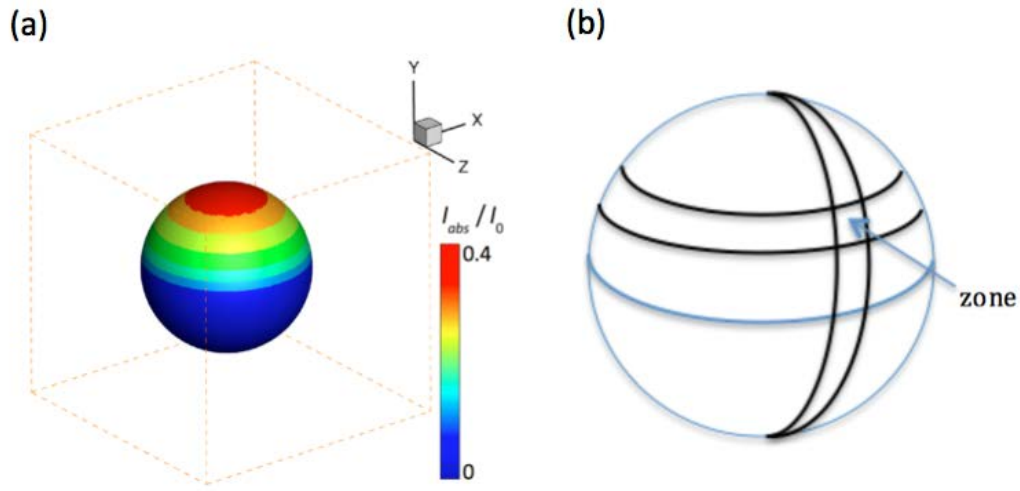

Fig. 3. Sensitivity analysis: (a) example of simulated power density by one particle; (b) definition of "zone".

The power density of each zone estimated by the simulation is compared with that calculated by the theory (Eqn. 4) based on the relative error as calculated in Eqn. 5,

$$E_r = \left| \frac{X - \bar{X}}{\bar{X}} \right| \tag{5}$$

, where X is the value of the term estimated by simulation and $\bar{X}$ is its theoretical value. Here X is $I_{abs,\,z}$ and $\bar{X}$ is $\bar{I}_{abs,\,z}$. The relative error should be reduced by using smaller ray size Δr for a certain zone area S_z. To determine the appropriate Δr according to S_z, simulations with different S_z and Δr are conducted as shown in Table 2. It is observed that the maximum relative error of $I_{abs,\,z}$ does converge as the ray size decreases (for a fixed zone area). For all the simulations in this paper the ray size is chosen according to Table 2 such that the maximum relative error is below 5%.

Table 2. Maximum relative error of using different zone areas and ray sizes

		Ray size (μm²)		
		0.02	0.015	0.01
Zone area (μm²)	8	8%	2.8%	1.4%
	2	3.5%	1.8%	0.9%
	0.5	37%	5%	2.5%

3.2 Model Validation

The ray tracing model is used to simulate the experiments in [19] for the purpose of model validation. In [19] a collimated laser beam passes through a small hole onto the PB. All the reflected radiation is then measured by a conic pyroelectric detector above the PB. The effective normal-hemispherical reflectance ρ_e is calculated as the ratio of total reflected power to incident laser power per unit surface from the experiment measurements.

First, the PACKS algorithm is used to generate the PB. The powder particle size distribution is assumed as Gaussian in this study, and the particle diameter is cut off at 3σ deviated from the mean. The thickness of the PB is made large enough such that the thickness does not affect ρ_e, as is the practice in the experiments. As shown in Table 3, the PACKS produces consistent relative density of PB with the experimental data, with a relative error less than 6%.

Table 3. Comparison of powder bed relative density between experiments and simulations

Material	Particle size (μm)	Experimental relative density	Simulated relative density	Relative error
Fe	125-160	0.55	0.55	0%
Fe	30-58	0.60	0.58	3.3%
Cu	125-160	0.58	0.55	5.2%

The ray tracing model is then used to simulate the laser absorption, from which the effective normal-hemispherical reflectance can also be quantified. To replicate the experiment conditions in the model, a laser beam of uniform power density distribution is shot on the PB contained in a cuboid CD; A laser diameter D_{laser} = 1000 μm is used so that the laser can cover up a significant amount of particles in the PB. Laser wavelengths of both 633 nm and 790 nm are used. The power coming out from the top of the CD is summed up, the ratio of which to the incident laser power is then compared with the ρ_e value obtained by experiments. The results are summarized in Table 4. There is a good agreement between simulations and experiments as the relative error of ρ_e is below 10% for all the cases.

Table 4. Comparison of effective normal-hemispherical reflectance ρ_e between experiments and simulations

Material	Particle size (μm)	Laser wavelength (nm)	Experimental reflectance [19]	Simulated reflectance	Relative error
Fe	125-160	790	0.243	0.264	8.6%
		633	0.228	0.246	7.9%
Fe	30-58	790	0.253	0.261	3.2%
		633	0.253	0.242	4.3%
Cu	125-160	790	0.709	0.748	5.5%
		633	0.641	0.654	2.0%

4 ANALYSIS AND DISCUSSION

The effects of laser parameters and PB structures are investigated based on different series of parametric studies, as listed in Table 5. In all of these simulations, the material of the

PB is stainless steel (SS), and the particles, unless specified otherwise, have a mean diameter d_m of 30 μm, a standard deviation σ of 5 μm, and the cut-off diameters of 15 μm and 45 μm. A fiber laser with the wavelength of 1070 nm is used for these studies.

Table 5. Total absorption, total absorption fluctuation, power density fluctuation, and surface roughness

		P_{total}/P_0 (%)	$\Delta P_{total}/P_0$ (%)	$\Delta I/I_0$ (%)	SR (μm)
Study 1: Effects of laser power profiles	a. Gaussian	65.20	1.73	67.34	13.67
	b. Top-hat	65.73	2.31	44.23	13.67
Study 2: Effects of laser absorptivity	a. Diffuse (SS)	64.99	2.30	43.33	13.67
	b. Angle-dependent (SS)	65.73	2.31	44.23	13.67
	a. Diffuse (Cu)	21.75	2.12	56.25	13.67
	b. Angle-dependent (Cu)	21.32	1.96	59.37	13.67
Study 3: Effects of laser spot size	a. D_{laser} = 30 μm	64.01	5.80	42.20	12.69
	b. D_{laser} = 60 μm	65.73	2.31	44.23	13.67
	c. D_{laser} = 150 μm	65.75	0.58	45.55	13.68
Study 4: Effects of powder bed thickness	a. t_{PB} = 60 μm	66.13	1.73	43.37	13.55
	b. t_{PB} = 90 μm	65.95	1.94	44.26	13.57
	c. t_{PB} = 180 μm	65.73	2.31	44.23	13.67
Study 5: Effects of substrate	a. With substrate	66.13	1.73	43.37	13.55
	b. Without substrate	58.22	2.35	48.75	13.55
Study 6: Effects of powder bed type	a. Unimodal	66.13	1.73	43.37	13.55
	b. Bimodal	63.64	1.43	38.87	4.51
Study 7: Effects of bimodal powder bed parameters	a. Bimodal PB1	63.64	1.43	38.87	4.51
	b. Bimodal PB2	62.49	1.41	40.55	4.61
	c. Bimodal PB3	63.84	1.30	31.80	2.65

Note:
P_{total} = Total absorbed power by the PB; P_0 = Laser power; ΔP_{total} = Fluctuation of total absorbed power by the PB; ΔI = Fluctuation of power density within the PB; I_0 = Laser power density; SR: denotes surface roughness.

4.1 Effects of Laser Power Profile

In Table 5 - Study 1 the top-hat and Gaussian laser power profiles are examined. A top-hat laser with radius of 30 μm and a Gaussian laser having a $1/e^2$ radius of 30 μm are shot on the same PB, respectively. The Gaussian laser is cut off at 1.52 of its $1/e^2$ radius and the power of both lasers is set to be the same. The thickness of the PB is 180 μm

In each ray tracing simulation there can be millions, if not more, incident points. To analyze the absorption distribution in a more efficient manner, the CD is divided into sub-domains, and the absorbed power in each sub-domain is calculated by summing up all the absorbed power within. The absorption distribution in the whole CD is, therefore, represented by the absorption in the sub-domains. Shown in Fig. 4a is an example of the CD in which a PB is

illuminated by a top-hat laser (I_{abs}/I_0 is the simulated normalized absorbed power density); the CD can be divided into sub-domains in the following manners:

- In Fig. 4b the top of the CD is divided into squares. Whenever the (x, z) coordinate of an incident point lies within a square, the absorbed power by this point is assigned to the square. The power density of a square is the absorbed power divided by the square area. By this fashion a power density distribution across the 2D-dimension transverse to the laser shooting direction can be constructed on the top of the CD. An example of the transverse power density distribution is already shown in Fig. 4b.
- In Fig. 4c the CD can be divided into layers along the laser shooting direction, which is denoted as the longitudinal direction (in opposed to the transverse directions). The absorbed power in each layer is calculated and a longitudinal power distribution can be obtained.
- In Fig. 4d the CD can also be divided into a series of annuli. The absorbed power in each annulus is calculated, and the power density for each annulus is calculated as the absorbed power in this annulus divided by its cross-section area vertical to the y axis. A radial power density distribution is therefore constructed.

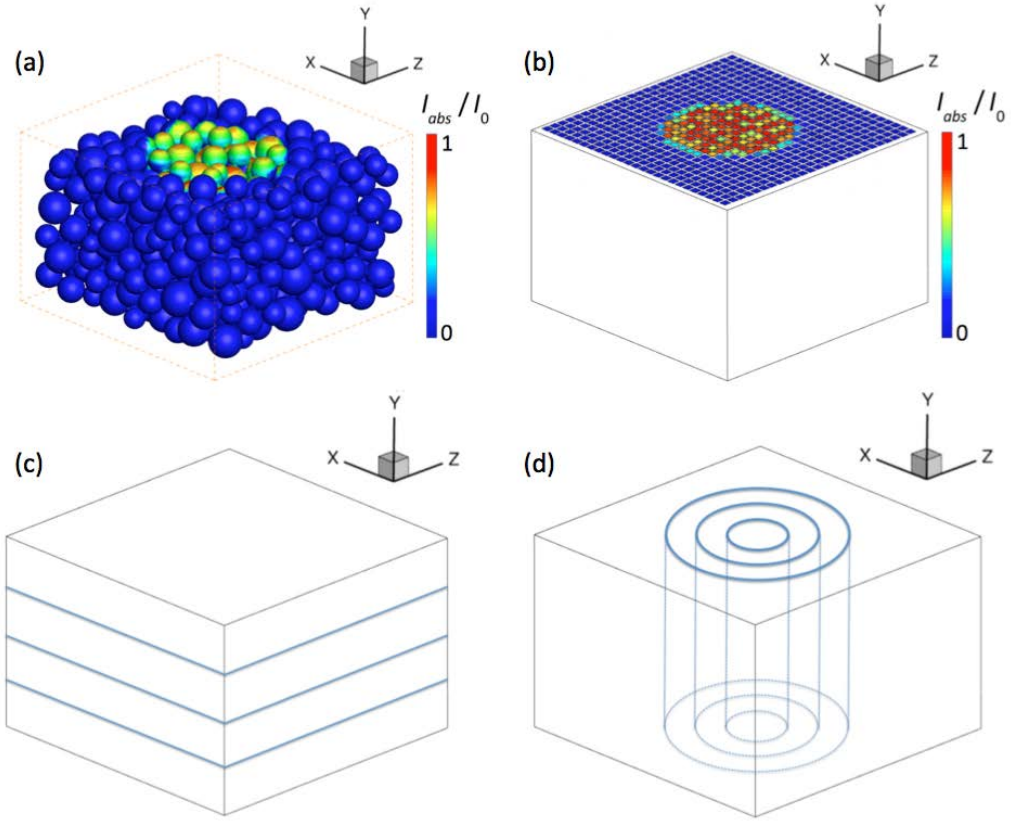

Fig. 4. Analysis of laser absorption distribution: (a) example of computational domain, powder bed structure and simulated absorption distribution for top-hat laser, (b) transverse power density distribution, (c) longitudinal power distribution, and (d) radial power density distribution.

The simulation results for different laser power profiles are summarized in Table 5 - Study 1. P_{total} is the average absorbed power of 30 simulations based on different PBs, and P_0 is the input laser power. The ratio of P_{total}/P_0 is used to quantify the (normalized) total absorption by the PB. ΔP_{total} is the standard deviation of the absorbed power from 30 PBs, and the ratio of

$\Delta P_{total}/P_0$ is used to quantify the total absorption fluctuation. As shown in Figure 4b, the power density in the laser spot fluctuates from square to square, which can cause inhomogeneous heating of the PB during SLS processes. Therefore, the ratio of $\Delta I/I_0$ is used to quantify the power density fluctuation within laser heated spots, in which ΔI is the standard deviation of power density of the square covered by the laser spot in all 30 PBs. Finally, the surface roughness (denoted as SR) is calculated as the standard deviation of the height of the PB surface. As will be mentioned in the studies to follow, SR can be used to indicate the unevenness of the PB surface, which can significantly affect the laser absorption. It is shown from Table 5 - Study 1 that the total absorption (65.20% vs. 65.31%) and its fluctuation (1.73% vs. 2.31%) are not significantly changed when different laser profiles are used. However, the top-hat profile gives much lower power density fluctuation (44.23%) than the Gaussian profile (67.34%). The SRs for the two cases are the same (13.68 μm) since identical PBs are used for different laser energy profiles.

The longitudinal and radial power density distribution for this study can be found in Fig. 5. Here P_{abs} denotes the absorbed power in each layer (as defined in Fig. 4c), and the ratio of P_{abs}/P_0 is the normalized absorbed power in the layer. The normalized absorption-in-layer is plotted as a function of layer depth in Fig. 5a. Also, I_{abs} denotes the power density of each annulus (as defined in Fig. 4d), and the ratio of I_{abs}/I_0, is the normalized power density in each annulus. The ratio is plotted as a function of annulus radius in Fig. 5b. The error bars in Fig. 5 plot the maximum and minimum values for the 30 simulations, which is an indicator of the uncertainty of the laser absorption caused by the randomness of the PB geometry. It is shown in Fig. 5a that the longitudinal power distributions are very similar even if different laser profiles are used. However, Fig. 5b shows quite different patterns of radial power density distribution between the top-hat and Gaussian profiles: the powder density is more uniform along the radial direction in the heated spot by top-hat lasers. This explains the reduction of power density fluctuation by top-hat laser, which is found in Table 5 - Study 1. It is, therefore, concluded that top-hat laser profile is superior to Gaussian profile in generating more uniform laser absorption within a laser heated spot.

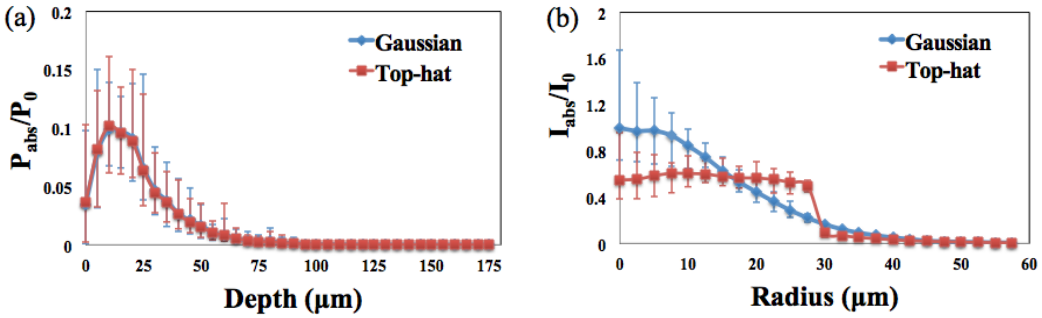

Fig. 5. Effects of laser power profile: (a) longitudinal power distribution and (b) radial power density distribution.

4.2 Effects of Laser Absorptivity

This paper adopts a laser absorptivity that is dependent on incident angle (Eqn. 3), while in other works [12-14] the absorptivity is assumed to be constant for all incident angles (diffuse

absorptivity). The difference between the diffuse absorptivity model and the "angle-dependent" model is, therefore, investigated. A top-hat laser with a 30 μm radius is shot on the PB consisting of SS or Cu particles, and then the absorption by the particles is calculated based on both the angle-dependent absorptivity and the diffuse absorptivity. The dependencies of absorptivity on the incident angle for both Cu and SS have already been shown in Fig. 2. In the diffuse model the absorptivity is calculated by Eqn. 6,

$$A_{diff} = \frac{2}{\pi}\int_0^{\pi/2} A(\gamma)d\gamma \qquad (6)$$

, where $A(\gamma)$ is the angle-dependent absorptivity calculated by Eqn. 3. The PB thickness used in this study is 180 μm. The simulation results are shown in Table 5 - Study 2 as well as Fig. 6 (for SS) and Fig. 7 (for Cu). It is found that the absorption distributions calculated by both models are similar, which can be easily understood with the help of Eqn. 4. The absorptivity is very different between these two models only when γ is close to 90 degrees (Fig. 2), but the rays with γ close to 90 degrees contribute little to the absorption since the multiplication of $A(\gamma)\cos\gamma$ is usually very small for those rays.

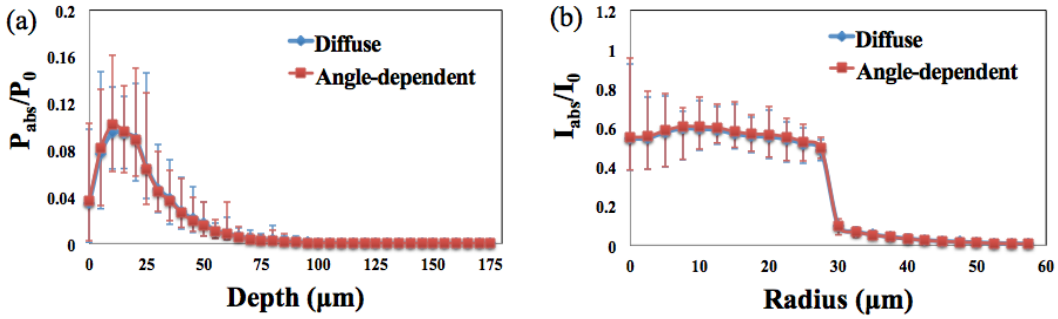

Fig. 6. Effects of laser absorption coefficient for stainless steel: (a) longitudinal power distribution and (b) radial power density distribution.

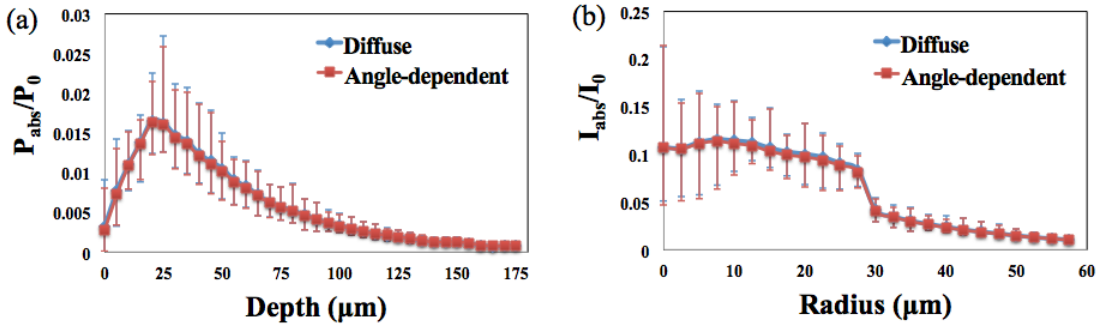

Fig. 7. Effects of laser absorption coefficient for copper: (a) longitudinal power distribution and (b) radial power density distribution.

SS has a moderate laser absorptivity while Cu has a very low absorptivity. It is interesting to compare the absorption patterns of these two materials. From Table 5 - Study 3 it is observed that the total absorption of SS is about 65%. This is close to the value of 60 % predicted in [11] and is almost twice the absorptivity by a flat surface of the same material (34% according to Fig. 2). The total absorption of the Cu PB is about 21%, which is nearly seven times that of Cu flat

surface (2.8% according to Fig. 2). The PB structure can better enhance the absorption for materials with low absorptivity. It is also observed by comparing Fig. 6a and Fig. 7a that a deep layer can share a larger portion of the total power absorption in the PB for the case of Cu PB, which indicates that the PB of low-absorptivity materials can have more laser penetration.

4.3 Effects of Laser Spot Size

Lasers of different diameters (30 μm, 60 μm, and 150 μm) are directed to the same PB of 180 μm thickness to study the effect of laser spot size. As shown in Table 5 - Study 3, the total absorption fluctuation, as an indicator of the variation of total absorption at 30 different laser heated spots, noticeably decreases as the laser spot becomes smaller, which is consistent with the findings in [11]. On the other hand, the power density fluctuation depicts the variation of absorption between different portions within a laser heated spot, and it is found that the laser spot size does not alter the uniformity of laser absorption within a laser heated spot.

The absorption profiles along longitudinal and radial directions are shown in Fig. 8. It is shown in Fig. 8a that similar longitudinal distributions of absorption for all laser spot sizes, but the error bars are generally longer for the curves with smaller laser spot sizes, indicating more fluctuation of absorption in their longitudinal distribution. Note that Fig. 8 shows very similar variation trend to those in Fig. 5a and Fig. 6a: as the layer depth increases, the absorbed power reaches a "peak" at several layers below the top surface and then decreases. Obviously the absorbed power does not decrease exponentially with the layer depth as assumed in [4, 13]. The absorption near the top of the PB is actually lower because more gaps exist between particles near the PB top and, therefore, fewer particle surfaces are available for laser absorption. This reveals the fact that the PB surface condition can affect the absorption: a looser PB surface tend to have more gaps between particles, leading to less power absorbed in the top layers and more power penetrating into the PB, and vice versa.

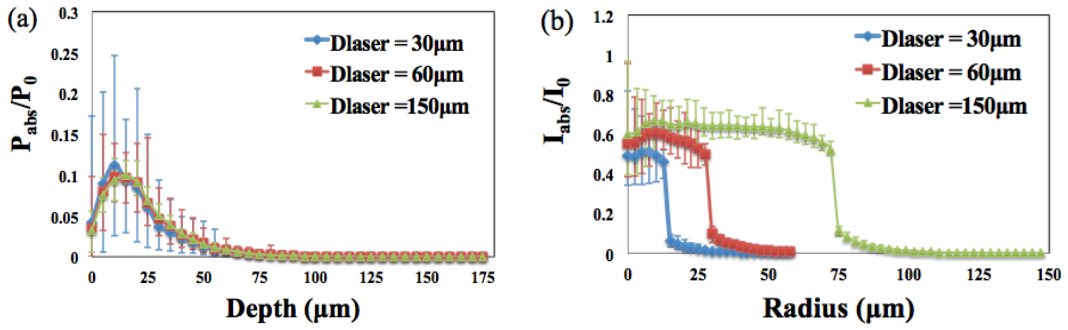

Fig. 8. Effects of laser spot size: (a) longitudinal power distribution and (b) radial power density distribution.

Fig. 8b shows the radial power density distributions with different laser sizes, all of which mimic the general profile of top-hat lasers. The length of the error bars is similar for all three cases, reaffirming that laser spot size does not significantly affect power density fluctuation (Table 5 - Study 3). The power density tends to decline near the edge of the laser spot before diving to a much lower value outside the spot. This is because in the center annulus there is an enhancement of absorption by the rays reflected from the neighboring annulus; while in the annulus near the laser spot edge there are almost no rays reflected from outside the laser spot.

Lasers with larger spot sizes are found to have a higher normalized power density for the same reason: at any location inside a larger laser spot, there are more surrounding regions from which the reflected rays can come in and enhance the local absorption.

4.4 Effects of Powder Bed Thickness

In the previous discussion, the PB is always thick enough (180 μm, equivalent to $6 \times d_m$) such that the effect of the substrate of the PB is negligible. However, in SLS processes the laser power is expected to penetrate the PB and reach the substrate underneath in order to bind the newly sintered layer with the substrate. The PB in SLS should be "thin" such that the absorption near the substrate is adequate. It is necessary then to study the absorption by thin PBs. To demonstrate the more remarkable influence of the PB substrate as the thickness decreases, simulations with different PB thicknesses (t_{PB} = 60 μm, 90 μm, and 180 μm) are conducted. The laser spot diameter is kept at 60 μm.

According to Table 5 - Study 4, the total absorption does not notably vary with t_{PB}, which is consistent with the results obtained in [13]. The radial absorption distribution (Fig. 9b) and power density fluctuation (Table 5 - Study 4) do not vary significantly with t_{PB} either. Fig. 9a shows the difference in longitudinal power distribution for different t_{PB}. There is a stand-alone point at the end of each curve to show the absorption by the PB substrate. The substrate absorption is quite noticeable when the PBs are thin (0.045 for t_{PB} = 60 μm, 0.013 for t_{PB} = 90 μm) and negligible when the PBs are thick (1.5e-5 for t_{PB} = 180 μm). In the meantime, the absorption at the bottom of the PB is also increased in thin PBs: in the very last layer above the substrate, the normalized absorbed power, P_{abs}/P_0, is 0.009 for t_{PB} = 60 μm, 0.001 for t_{PB} = 90 μm and 1e-5 for t_{PB} = 180 μm.

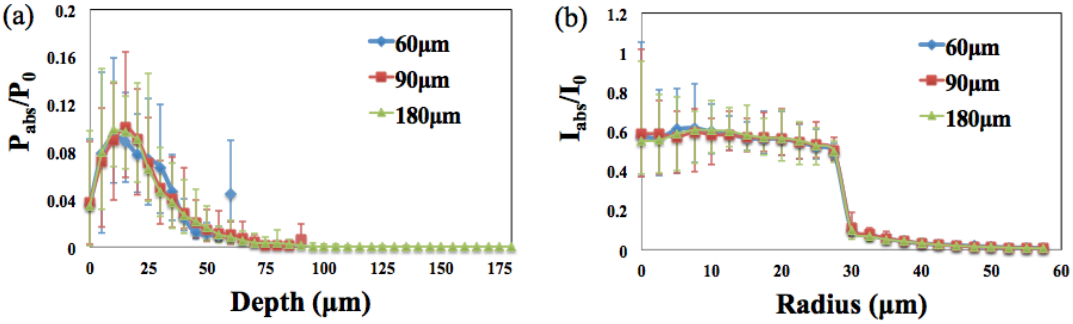

Fig. 9. Effects of powder bed thickness: (a) longitudinal power distribution and (b) radial power density distribution.

The PB thickness of 60 μm is chosen as a typical value for a thin PB used in the current work. The effects of the substrate are explicitly demonstrated by the following simulations. Two cases are calculated: one case accounts for the absorption and reflection of the substrate as before, and in the other case the rays are assumed to pass through the substrate without being reflected (so that the effects of the substrate are excluded). The laser diameter is still 60 μm. It is found that the total absorption is increased by 6% with the substrate (Table 5 - Study 5), and the absorbed power in layers near PB bottom is increased (Fig. 10a) due to the laser reflected from the substrate. There are also reductions in total absorption fluctuation and power density

fluctuation for the case with the substrate (Table 5 - Study 5). This study shows that the substrate can both enhance and uniform the absorption in the PB.

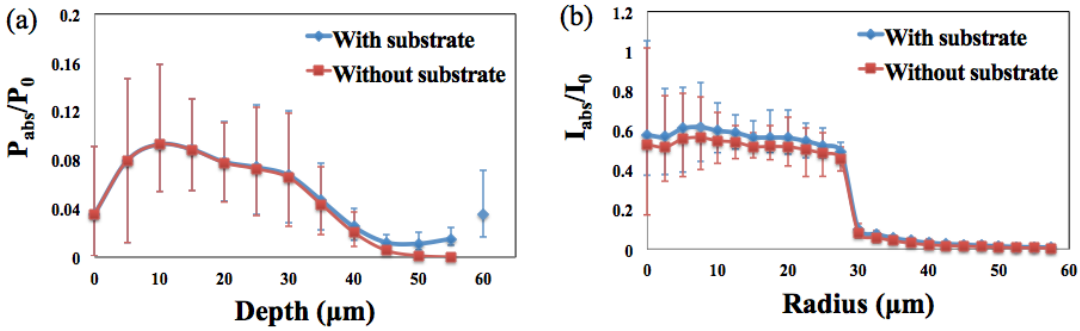

Fig. 10. Effects of substrate: (a) longitudinal power distribution and (b) radial power density distribution.

4.5 Effects of Bimodal Powder Bed

The absorption in the bimodal PB is of particular interest to SLS processes. It is pointed out that bimodal PB can increase laser absorption [11] and help to avoid the balling phenomenon [12]. In this paper, bimodal PBs are generated by mixing particles of two Gaussian size distributions, one for "big" particles and the other for "small" particles. The size of big particles is 15-45 μm. The size of small particles and their volume percentage in the feedstock are listed in Table 6. The bimodal PB thickness is fixed at 60 μm to simulate the cases of thin PB, which are the more realistic scenarios in SLS.

Table 6. Bimodal powder bed parameters

	Small particle size (μm)	Volume percentage of small particles in feedstock
Bimodal PB1	9-11	20%
Bimodal PB2	9-11	5%
Bimodal PB3	5-7	20%

The volume percentage of small particles in the PB can actually be higher than that in the feedstock. In an SLS process, a PB is generated by dumping more-than-enough powders on the substrate and using a roller (or doctor blade) to create a desired PB thickness. When the roller passes by above the PB, particles can be wiped away if they cannot secure a position below the desired PB thickness. Small particles can fill in the voids between big particles in the PB, and hence have a greater chance of staying in the PB without being wiped away, increasing their volume percentage in the PB. As will be discussed later, this phenomenon can have significant effects on the PB absorption.

First, the differences of absorption by bimodal and unimodal (i.e. with only one particle size distribution) PBs are examined by comparing bimodal PB1 in Table 6 and a unimodal PB consisting of only the big particles. The laser diameter is fixed at 60 μm. As shown in Fig. 11a: the longitudinal power absorptions by the bimodal PB and the unimodal PB are very different. In the bimodal PB the small particles tend to fill the voids created by big particles, leading to a very

densely packed PB surface (compare Fig. 12a and Fig. 12b). Most of the power absorption takes place on the densely packed particles near the PB surface, leading to a high absorption peak in the top layers; less laser power is able to penetrate into the PB, leading to low absorption in the bottom layers. In the unimodal PB the surface is loosely packed and hence the longitudinal power distribution curve is "flat".

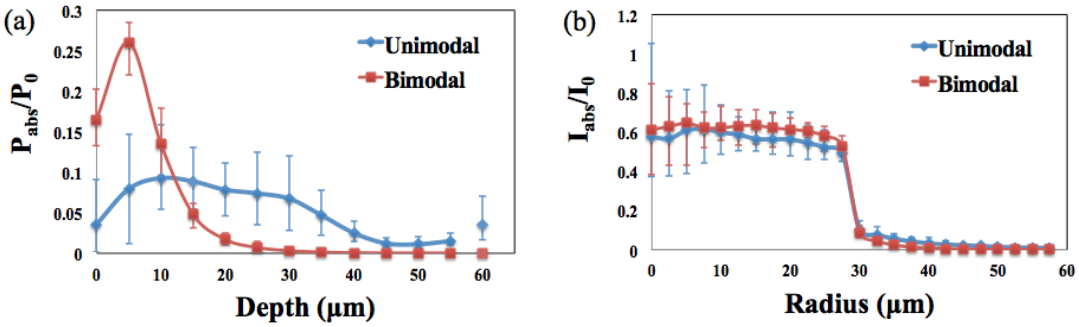

Fig. 11. Effects powder bed type: (a) longitudinal power distribution and (b) radial power density distribution.

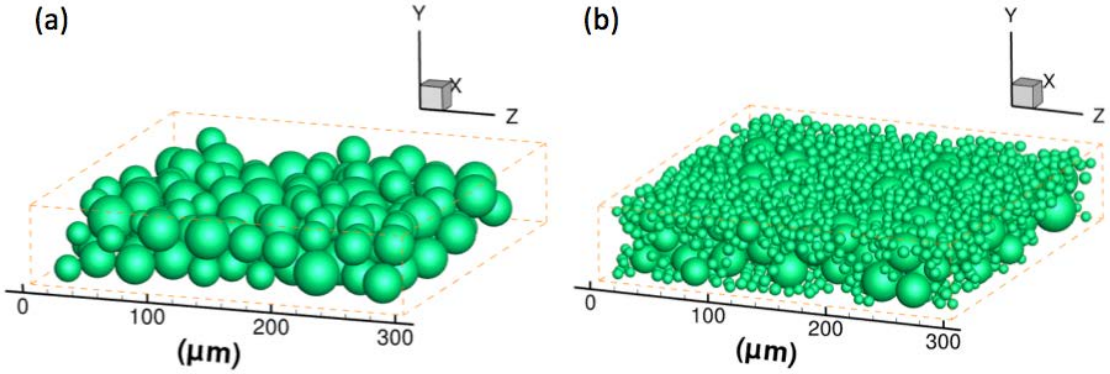

Fig. 12. Example of: (a) unimodal powder bed and (b) bimodal powder bed.

It is also noticed that in Table 5 - Study 6 the power density fluctuation is smaller in the bimodal PB. This could be attributed to the evener PB surface due to small particles filling in the voids in bimodal PBs. As can be seen in Table 5 - Study 6 that the surface roughness for bimodal PB (4.51μm) is nearly one-third of that of unimodal PB (13.55μm). The comparison between unimodal and bimodal PBs shows that the small particles in a bimodal PB can significantly change the surface conditions of a PB, and hence the absorption distribution becomes dramatically different from that of a unimodal PB. This suggests that the surface conditions of a PB can significantly affect the absorption distributions.

To study the bimodal PB absorption more thoroughly, the effects of the volume fraction of small particles in the feedstock are examined in Table 5 - Study 7. Bimodal PB1 and PB2 have the same small particle size but different small particle volume percentages. Given more-than-enough powders in the feedstock, the small particles will always generate a very densely packed PB surface regardless of their volume fraction in the feedstock. Since the surface conditions of PB can dominate the absorption distribution, few differences can be expected

between these two bimodal PBs in their longitudinal power distributions and radial power density distributions, as shown in Fig. 13, and all the absorption data in Table 5 - Study 7 are also similar.

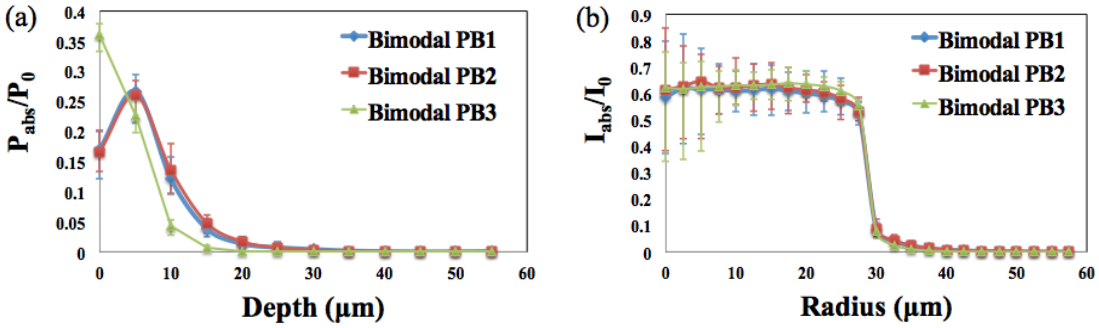

Fig. 13. Effects bimodal powder bed parameters: (a) longitudinal power distribution and (b) radial power density distribution.

The effects of the small particle size are also studied by comparing the absorption by bimodal PB1 and PB3; bimodal PB3 has the same volume fraction but a smaller size for the small particles in the feedstock (Table 6). As shown in Table 5 - Study 7 the surface roughness of bimodal PB3 (2.65μm) is nearly half of that of bimodal PB1 (4.51μm), which means the surface of bimodal PB3 is evener and more densely packed. Again, since the surface condition can dominate the absorption distribution, a further lack of power penetration can be expected in the longitudinal power distribution in bimodal PB3, as in Fig. 13a the "peak" below the PB surface disappears and the absorption in the very top layer is the highest. It is also expected that in Table 5 - Study 7 the power density fluctuation is smaller for bimodal PB3 due to an evener PB surface.

5 CONCLUSIONS

In this paper, randomly packed powder beds are generated by The Probabilistic-Analytic Consecutive Kinetic Simulation (PACKS), and then a ray tracing model is used to simulate the laser absorption by powder bed in selective laser sintering (SLS) processes. A criterion to choose the ray size to ensure model accuracy is proposed, and the results of the PACKS and the ray tracing model are validated against experimental data. Parametric studies are conducted to investigate the effects of laser parameters and powder bed structures on laser absorption, and the following major conclusions are made:

- Top-hat laser is superior to Gaussian laser in producing more uniform absorption in the powder bed.
- The powder bed structure can have higher laser absorption and deeper laser penetration than a flat surface structure. These effects are more significant for materials with low absorptivity.
- The absorption distribution along the laser shooting direction does not follow an exponential decay. Instead, absorption generally first increases until it reaches a "peak" and drops steeply after that. For top-hat lasers, the radial power density distribution tends to decrease near the edge of the laser spot before a dive into a much lower value outside the laser spot.

- The thin powder bed has higher absorption near the substrate. The total absorption of thin PBs is of the same magnitude as those of thick PBs due to the enhancing effect of the substrate.
- Compared with unimodal powder beds, bimodal powder beds have evener and more densely packed surfaces. Such changes in powder bed surfaces can increase the surface absorption and reduce laser penetration into the powder beds. The laser absorption can also be more uniform in bimodal powder beds.

REFERENCE:

[1] Gibson I, Rosen DW, and Stucker B, "Additive manufacturing technologies," *Springer, New York,* 2010.

[2] N. Hodge, R. Ferencz, and J. Solberg, "Implementation of a thermomechanical model for the simulation of selective laser melting," *Computational Mechanics,* vol. 54, pp. 33-51, 2014.

[3] A. Gusarov and J.-P. Kruth, "Modelling of radiation transfer in metallic powders at laser treatment," *International Journal of Heat and Mass Transfer*, vol. 48, pp. 3423-3434, 2005.

[4] J. Yin, H. Zhu, L. Ke, P. Hu, C. He, H. Zhang, and X. Zeng, "A finite element model of thermal evolution in laser micro sintering," *The International Journal of Advanced Manufacturing Technology,* vol. 83, pp. 1847-1859, 2016.

[5] S. A. Khairallah, A. T. Anderson, A. Rubenchik, and W. E. King, "Laser powder-bed fusion additive manufacturing: Physics of complex melt flow and formation mechanisms of pores, spatter, and denudation zones," *Acta Materialia,* vol. 108, pp. 36-45, 2016.

[6] H. Ki, J. Mazumder, and P. S. Mohanty, "Modeling of laser keyhole welding: Part I. Mathematical modeling, numerical methodology, role of recoil pressure, multiple reflections, and free surface evolution," *Metallurgical and materials transactions A,* vol. 33, pp. 1817-1830, 2002.

[7] H. Ki, P. S. Mohanty, and J. Mazumder, "Multiple reflection and its influence on keyhole evolution," *Journal of laser applications,* vol. 14, pp. 39-45, 2002.

[8] W. Tan, N. S. Bailey, and Y. C. Shin, "Investigation of keyhole plume and molten pool based on a three-dimensional dynamic model with sharp interface formulation," *Journal of Physics D: Applied Physics,* vol. 46, p. 055501, 2013.

[9] W. Tan and Y. C. Shin, "Analysis of multi-phase interaction and its effects on keyhole dynamics with a multi-physics numerical model," *Journal of Physics D: Applied Physics,* vol. 47, p. 345501, 2014.

[10] W. Devesse, D. De Baere, and P. Guillaume, "Modeling of laser beam and powder flow interaction in laser cladding using ray-tracing," *Journal of Laser Applications,* vol. 27, p. S29208, 2015.

[11] C. Boley, S. Khairallah, and A. Rubenchik, "Calculation of laser absorption by metal powders in additive manufacturing," *Applied optics,* vol. 54, pp. 2477-2482, 2015.

[12] J. Zhou, Y. Zhang, and J. Chen, "Numerical simulation of laser irradiation to a randomly packed bimodal powder bed," *International Journal of Heat and Mass Transfer,* vol. 52, pp. 3137-3146, 2009.

[13] D. Moser, S. Pannala, and J. Murthy, "Computation of Effective Radiative Properties of Powders for Selective Laser Sintering Simulations," *JOM,* vol. 67, pp. 1194-1202, 2015.

[14] A. Streek, P. Regenfuss, and H. Exner, "Fundamentals of energy conversion and dissipation in powder layers during laser micro sintering," *Physics Procedia,* vol. 41, pp. 858-869, 2013.
[15] R. Siegel and J. R. Howell, "Thermal radiation Heat Transfer. 2nd," *Hemisphere, Washington DC,* 1981.
[16] W. S. Jodrey and E. M. Tory, "Simulation of random packing of spheres," *Simulation,* vol. 32, pp. 1-12, 1979.
[17] A. Kaplan, "Laser absorptivity on wavy molten metal surfaces: Categorization of different metals and wavelengths," *Journal of Laser Applications,* vol. 26, p. 012007, 2014.
[18] M. A. Ordal, R. J. Bell, R. W. Alexander, L. A. Newquist, and M. R. Querry, "Optical properties of Al, Fe, Ti, Ta, W, and Mo at submillimeter wavelengths," *Applied optics,* vol. 27, pp. 1203-1209, 1988.
[19] A. Gusarov, E. H. Bentefour, M. Rombouts, L. Froyen, C. Glorieux, and J.-P. Kruth, "Normal-directional and normal-hemispherical reflectances of micron-and submicron-sized powder beds at 633 and 790nm," *Journal of applied physics,* vol. 99, p. 113528, 2006.